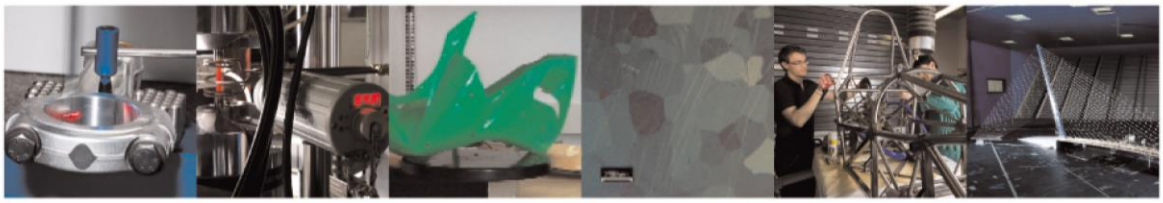

Influence of the atomization medium on the properties of stainless steel SLM parts

S. Cacace, Q. Semeraro

This is a post-peer-review, pre-copyedit version of an article published in Additive Manufacturing. The final authenticated version is available online at:
http://dx.doi.org/10.1016/j.addma.2020.101509

DIPARTIMENTO DI MECCANICA ■ POLITECNICO DI MILANO
via G. La Masa, 1 ■ 20156 Milano ■ EMAIL (PEC): pecmecc@cert.polimi.it
http://www.mecc.polimi.it
Rev. 0

Influence of the atomization medium on the properties of Stainless Steel SLM parts

S. Cacace[a,*], Q. Semeraro[a]

[a] *Dipartimento di Meccanica, Politecnico di Milano, Via La Masa 1, 20156 Milano, Italy*

Abstract

The importance of powders on the final part properties in Selective Laser Melting (SLM) process is well-known. At the moment, gas atomization is used to produce powders for the SLM process. However, there is a growing interest in investigating the use of the less expensive water atomization process. In this work, water and gas atomized powders were used as feedstock to produce specimens with an industrial SLM system. First, the influence of particle size distribution and layer thickness on the final part density was studied by varying process parameters by means of a factorial design. The results showed that by using a particle size distribution in the range 15 - 60 µm the difference in part density between water and gas atomized is negligible even using the same combination of parameters. The tensile properties of GA and WA powder are comparable: respectively 599 and 601 MPa for the ultimate tensile strength, 18% and 20% for the elongation.

Keywords:

Selective Laser Melting, Atomization, Stainless Steel

*Corresponding author

Email address: stefania.cacace@polimi.it (S. Cacace)

1. Introduction

Selective Laser Melting (SLM) is a well-known powder-based additive manufacturing technique allowing the production of parts directly from 3D CAD models. In recent years, several studies investigated the influence of process parameters on the SLM final part properties, [1],[2], [3] and [4] to cite a few. The most studied parameters are usually laser-related process parameters, such as laser power, scan speed or scanning properties, such as hatch distance. It is also well known that powder characteristics have a major influence on the final part and that their properties might depend on the production process used. At present, SLM machine manufacturers suggest using spherical particles produced with gas atomization (GA). GA process produces almost spherical particles with a good chemical purity [5], [6] and [7]. However, there is a growing interest in less expensive powder production processes with the aim of reducing the production costs for SLM parts, for example water atomization (WA). WA and GA powders differ in terms of the geometry of the particles and the chemical composition. WA powders are highly irregular and are characterized by higher oxygen content [8], [9]. Studying the effect of the production process has the objective of both verifying the opportunity to produce parts with good mechanical properties by means of less expensive powders and, also investigating the effect of different powder properties on SLM parts. The cost of stainless steel powders could be reduced to a fifth using water atomization rather than gas atomization. In breaking down the cost of a reference part, [10] found that the cost of the material constitutes up to 11 % of the overall batch cost. Lindemann work, while dated, considers stainless steel material and a cost per kg similar to the commercial powder used in this work. More recently,

Baumers et al. [11] provided an estimation of the breakdown cost for SLM considering 17-4PH steel. The material cost impact on the printed part was slightly higher than 10%. The cost of gas atomized 316L powders with a particle size distribution in the range 15 -50 μm is about 60 €/kg. WA powders for the same particle range cost around 15 €/Kg (estimation based on a private communications with a potential manufacturer). Considering a 10% impact of the material cost on the production of the part, using WA could lead to a reduction in the production cost close to 8% .

In this work, WA and GA stainless steel AISI 316L powders with different particle size distributions were analyzed and used in an industrial SLM system. The part density was investigated by varying process parameters. Eventually, the best combination of parameters for each powder was determined; the optimal condition was used to study the tensile properties of WA and GA powders. The paper is organized as follows: in Section 2 the state of the art is presented. The description of the SLM machine, sample and powder characterization techniques are described in Section 3. Afterward, the powder characterization is described in Section 4 and, eventually, density and tensile properties are reported and discussed in Section 5.

2. State of the art

The state of the art is divided into two sections. The first one deals with the different powders that can be used in Selective Laser Melting process, the second part focuses on the relationship between particle size distribution and layer thickness values.

2.1. Gas and water atomized powders

In the SLM industry, the powders used are generally produced with gas atomization processes. GA powders are spherical, with relatively smooth surfaces and good chemical purity [12]. These properties are supposed to give higher powder bed density, which should enhance the SLM part performances. However, GA powders are also characterized by internal porosity, which might induce defects on the final part [13] and the presence of satellites on the surface is supposed to reduce the flowability. The use of GA as the production process is also due to the large range of materials available. Despite the advantages of the GA process, lately, a growing interest for other powder production processes was observed for SLM applications. In particular, WA powders have been investigated to study how they behave in powder bed additive processes. The interest in WA powders is due to the lower cost, compared to GA for the same material. In recent years, the use of WA powders as raw material for the SLM process was investigated in the literature. In Table 1, the research works on the use of WA and GA powders in SLM are summarized. Works by Engeli et al.[9] and Olakanmi [14] showed that localized porosities in the final samples can be related to the low powder flow in irregular WA particles. Irregular particles have also lower packing density compared to spherical ones. The combination of lower flowability and lower packing densities has negative effects on the homogeneity of the powder layer resulting in higher porosity content and lower mechanical properties for WA samples [9]. Irrinki et al.[8] obtained a density up to 97.5% using both GA and WA 17-4 PH powders and WA samples obtained the same mechanical properties compared to GA samples when processed at high energy density. They used three WA powders characterized by different particle size distributions (PSD); the coarser batch

obtained the best performances at high energy density values, consistently with the work of [15] using GA powders. The results by Olakanmi [14] using Al alloys powders proved that it is possible to obtain good processability of irregular particles at high levels of energy density, i.e. low scan speed. Letenneur et al. [16] used two batches of WA Iron powders to produce density and tensile specimen; they managed to obtain very high density ($> 99\%$) and high tensile properties. In [17], the authors used WA and GA stainless steel powders at different speed levels; the preliminary result showed that GA samples reached higher density values and were less subjected to balling phenomena compared to WA parts.

In conclusion, by looking at Table 1 we can see that:

- the materials used are different and it is not advisable to compare these results
- most of the papers consider part density as final part property, and few works perform tensile tests
- the experimental design are quite poor, only few works change process parameters

2.2. Particle size distribution and layer thickness

The choice of process parameters should be based on the information available on the powder properties. The interaction between PSD and the layer thickness (z) of the process is of great interest for industrial purposes. The reason for this interest is due to the fact that the layer thickness is an important driver for productivity: the layer thickness level should be chosen to maximize the productivity ensuring bonding between consecutive layers. According to Spierings et al. [18], the effective layer thickness should be

higher than the PSD 90th percentile, so that big particles are deposited on the powder bed rather than removed by the rake. Guan et al. [19] used a 304 AISI powder with a particle size distribution lower than 50 m (the mean particle size was 20 m) . The authors obtained good mechanical properties using layer thickness values of 20, 30 and 40 μm, while at 50 μm the balling effect prevented building the parts. On the contrary, Ma et al. [20] obtained good final part properties using layer thicknesses up to 100 m, which is almost twice the largest diameter of the powder, equal to 60 m. Hu et al. [21] and Sufiiarov et al. [22] obtained results that are in line with the works by [18] where the optimal layer thickness was found to be smaller than the largest diameter of the powder. Alfaify et al. [15] processed three different Ti6Al4V powders and the results showed that it was possible to obtain high density for powders with differente PSD using three levels of layer thickness (60, 80 and 100 μm).

Looking at Table 2, it is clear that almost all papers agree on choosing a layer thickness smaller than or equal the D(90) of the particle size distribution. Two papers varied both particle size distribution and layer thickness, [15] and [18]. The reported results are contrasting as [15] showed that it was possible to obtain high density also when the layer thickness was half the size of the D(90), while for [18] there is a limit on the maximum particle size depending on the layer.

Table 1: State of the art on WA powders in SLM. The number of powders used for each production process is reported in round brackets.

Paper	Material	Production process	Experimental Parameters	Measured outputs	Results
[8]	17-4PH	GA (1), WA (3) GA (1)	P = {150;195} W; v = {1250; 1550} mm/s	Mean density; tensile properties; hardness	WA samples obtained similar tensile properties when processed at high energy density
[9]	IN718	GA (7) , WA (1)	Same process parameters for all batches	Mean density	WA sample had higher porosity than GA samples.
[14]	Al, Al-Si	GA pure Al (1); WA Al 5.7 Mg (1), WA Al-6Mg (1), GA Al-12Si (1)	P = 150 W, v = 80-200 mm/s	Mean density	Similar processing maps despite different chemical composition and powder production process
[16]	Iron	WA (2)	v = 400-1200 mm/s; P = 170-370 W	Mean density; tensile properties; three point bending test; dimensional accuracy; surface roughness	High part density and good mechanical properties were obtained using WA powders. The influence of process parameters on the mechanical properties were evaluated.
[17]	AISI 316L	GA (2), WA (2)	v = 100-180 mm/s µm	Mean density	GA powders performed better than WA in all conditions

Table 2: State of the art on layer thickness z and particle size distribution in SLM. The number of powder used for each production process is reported in round brackets.

Paper	Material	PSD (µm)	Experimental parameters	z (µm)	Measured outputs	Results
[15]	GA Ti6Al4V (3)	D(10)-D(90): 20.6-48.6; 43.2-81.2; 51.7-105;	layer thickness, exposure time	60, 80, 100 µm	Mean density	A thinner layer allows to obtain high density at a low value of energy density.
[18]	GA 316L (3)	D(10)-D(90): 71–24.17; 19.84-41.13; 15.26-55.54	Scan speed	30, 45 µm	Surface roughness, mean density, tensile properties	z influences surface roughness. There is a limit on the size of particles depending on z.
[19]	GA AISI 316L (1)	D(50)=20 µm, D(90)=50 µm	Not varied	20, 30, 40	Tensile properties	All z levels resulted in similar tensile properties
[20]	GA 1Cr18Ni9Ti (1)	D(90) $<$ 60 µm	Scan speed	60, 80, 100, 120, 150	Mean density, tensile properties, microhardness	Good properties for z$<$100 µm.
[21]	GA 17-4PH (1)	D(10)-D(90): 10-74 µm	Scan speed, hatch distance	20, 30, 40	Mean density, tensile properties, porosity	smaller layer thickness increases density
[22]	GA Inconel 718	D(10)-D(90): 15.5-57.6 µm	Power, scan speed, hatch distance	30, 50	Mean density, tensile properties	Smaller layer thickness improves mechanical properties.

In this work, the influence of powder production process on SLM final part is investigated. Stainless steel powders produced with gas atomization and water atomization processes were used; for each production process, two particle size distributions were considered. An experimental campaign was designed to study the influence of SLM process parameters and volumetric energy density on part density. The experimental campaign was divided into two stages. In the first part, a factorial design was used to determine SLM optimal processing conditions, by varying layer thickness, particle size distribution and process parameters for both WA and GA powders. At a second stage, the best condition for WA and GA powders was used to produce tensile specimen and to compare static properties.

3. Experimental setup

3.1. Selective laser melting machine

All experiments were conducted using a Renishaw AM250 industrial machine. The machine uses a 200 W fiber laser working in pulsed mode. Prior to processing, vacuum is applied to the working area until the oxygen content is lower than 1000 ppm. During the process, the chamber is filled with a constant Argon gas flow. In order to mak it possible to use a small amount of different powders, the Renishaw machine was equipped with the RBV system (Reduced Build Volume). The RBV system allowed us to use the same laser of the Renishaw machine and all the equipment for the atmosphere control.

3.2. Mechanical characterization

For the density measurements, an electronic scale (Precisa 100A-300 M) with a kit for the density measurement was used (Sartorius YDK 01) . To

calculate density, , the following formula was used:

$$\rho = \frac{W_a \cdot \rho_{fl}}{W_a - W_{fl}} \tag{1}$$

where W_a is the weight of the specimen in air [g], W_{fl} is the weight of the specimen in water [g] and ρ_{fl} is the density of the water [g/cm^3]. During the measurement water temperature, air temperature and air pressure were constantly measured. The measurements were conducted in deionized water and the temperature dependence of water density with the temperature was considered. Each sample is measured three times in water and three times in air in a randomized order. The final density is the mean results of the three replicates. Cylindrical samples with 5 mm diameter and 12 mm height were produced to characterize the density. The reference values used for the density of 316L is 7.98 g/cm^3.

Tensile tests were performed at room temperature using a MTS Alliance RF/100. Tests were performed with an initial speed of 0.4 mm/min and a secondary speed of 2 mm/min. The removal point was set at 0.16 mm. An MTS 632 26F-20 extensometer with a gauge length of 8 mm was used. The tensile tests were performed according to ASTM E8 -16 standard. The tensile specimen dimensions are reported in Table 3. Tensile specimens were tested in "as-built" condition without any post-processing, such as sand-blasting or machining.

Table 3: Tensile test specimen geometry according to ASTM E8.

Dimension (mm) for tensile test specimen	
G - Gauge length	16.0 ± 0.1
D - Diameter	4.0 ± 0.1
R radius of fillet min	4
A - length of reduced section, min	21

Carl Zeiss EVO-50 scanning electron microscope was also used to examine cross sections and fracture surfaces of the tensile specimens.
Samples of interest were scanned using X-ray computed tomography with NSI X25 system (North Star Imaging X25); the reconstruction software is efX-DR provided by NSI. Pores size and shape are analyzed with a self-developed Matlab code. The voxel size is 6.2 x 6.2 x 6.2 μm^3.

3.3. Powder characterization

Water atomized and gas atomized AISI 316L stainless steel powders were used in this work. A special production of water atomized powders was provided by Pometon S.p.A (Italy) and commercially available gas atomized powders were used. For each type of powder, two different particle size distributions are available. Powder size distributions were analyzed using a Malvern Mastersizer 2000 laser diffraction machine. For chemical composition, the Oxygen level was measured with Inert Gas Fusion method (ISO 4491-4). Apparent density was measured according to ASTM B212-13 standard.

3.4. Design of the experiment

Exposure time t, hatch distance d_h, point distance d_p and layer thickness z were varied to study their influence on the densification of the different powders. Power P was kept constant for all the experiment and equal to 200 W to maximize productivity.

Exposure time is defined as the duration of the laser emission on a single spot, point distance is the distance between two consecutive spots on the same scan line and hatch distance is the distance between two consecutive scan lines. The levels of parameters t, d_p and d_h were chosen to obtain the same interval of volumetric energy density for the two levels of layer thickness considered, z = 50 µm and z = 75 µm. Volumetric energy density (E_d) in J/mm^3 is defined as:

$$E_d = \frac{P \cdot t}{d_h \cdot d_p \cdot z} \tag{2}$$

The choice of the parameters to process the two powders was made starting from the Renishaw suggested conditions for AISI 316L, reported in Table 4.

Table 4: Renishaw suggested parameters for AISI 316L for z = 50 µm.

t, µs	**d_p**, µm	**d_h**, µm	**z**, µm	**E_d**, J/mm³
80	60	100	50	53.33

Two 2^3 designs were implemented, one for each level of layer thickness 50 µm and 75 µm. Using the condition in Table 4 as a center point, a first 2^3 factorial design was created for layer thickness 50 µm. The experimental conditions are reported in Table 5. The low and high levels of each parameter were chosen as -10% and +10% of the center point. This choice was

performed to avoid under-melting or over-melting conditions [23].

Table 5: 2^3 factorial design for layer thickness 50 µm. Power is constant for all conditions and equal to 200 W.

t, µs	$\mathbf{d_p}$, µm	$\mathbf{d_h}$, µm	$\mathbf{E_d}$, $^{J}/_{mm^3}$
72	54	90	59.3
88	54	90	72.4
72	66	90	48.5
88	66	90	59.3
72	54	110	48.5
88	54	110	59.3
72	66	110	39.7
88	66	110	48.5

The process parameters from Table 5 were scaled to obtain the same volumetric energy density for a layer thickness of 75 µm; the results are in Table 6 (center point) and Table 7 (2^3 factorial). The scaling factor is equal to $\left(\frac{75}{50}\right)^{1/3}$.

Table 6: Renishaws suggested processing conditions for AISI 316L scaled for layer thickness 75 µm.

t, µs	$\mathbf{d_p}$, µm	$\mathbf{d_h}$, µm	**z**, µm	$\mathbf{E_d}$, $^{J}/_{mm^3}$
91.55	52.45	87.35	75	53.33

Table 7: 2^k factorial design scaled for layer thickness 75 µm. Power is constant for all the conditions and equal to 200 W.

t, µs	$\mathbf{d_p}$, µm	$\mathbf{d_h}$, µm	$\mathbf{E_d}$, $^{J}/_{mm^3}$
82	47	79	59.3
101	47	79	72.4
82	58	79	48.5
101	58	79	59.3
82	47	96	48.5
101	47	96	59.3
82	58	96	39.7
101	58	96	48.5

For each combination of powder and layer thickness, a different build was made, so the total number of builds is equal to 8 (2 powder production processes $\times$ 2 particle size distributions $\times$ 2 layer thicknesses). The list of builds is reported in Table 8. In every build, the 2^3 factorial design was replicated twice and the center point six times. The total number of samples produced in each build is equal to $2^3 \times 2 + 6 = 22$. In conclusion, 176 samples were produced for density evaluation.

Table 8: List of builds for the experimentation.

Build name	**Powder**	**Granulometry**	**Layer thickness**, µm
B1	WA	Fine	50
B2	WA	Fine	75
B3	WA	Coarse	50
B4	WA	Coarse	75
B5	GA	Fine	50
B6	GA	Fine	75
B7	GA	Coarse	50
B8	GA	Coarse	75

4. Powder characterization

In Table 9 and in Figure 1 particles size distribution quantiles and cumulative distributions are showed, while in Figure 1 SEM images are reported. The chemical composition of the four powder batches is summarized in Table 10.

Table 9: Characteristic values for the particle size distribution and apparent density for the four powders.

Production process	**Granulometry**	**D10**, µm	**D50**, µm	**D90**, µm	**Apparent density**, g/cm^3
GA	Fine	19.4	34.6	56.8	4.07
WA	Fine	20.0	40.0	69.7	3.15
GA	Coarse	76.8	107.0	149.0	4.20
WA	Coarse	53.0	91.0	151.0	3.14

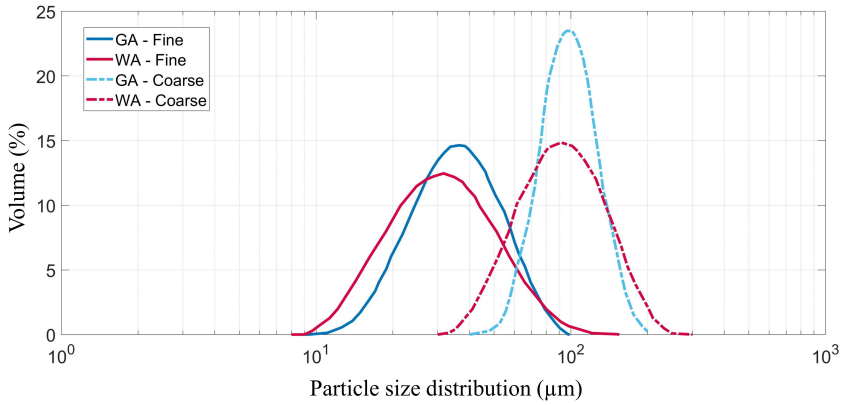

Figure 1: Particle size distribution for all powders.

The particle size distributions of fine fractions are comparable for both WA and GA powders, even if the 90^{th} quantile of WA is larger. As a matter of fact, the spans of the two distributions (evaluated as [D(90)-D(10)]/D(50)) are similar. Conversely, coarser fractions have different distributions; in

detail, GA powders have a smaller span compared to WA as the 10^{th} of the WA powder is finer. Apparent density for all powders was evaluated according to ASTM B212-13 standard. GA powders have higher apparent density than WA, this result was also obtained by Irrinki et al. [24] and Engeli et al. [9]. Apparent density is affected by powder shape and particle size distribution, spherical powders show higher apparent density values.

Table 10: Chemical composition for all the powders used.

Powder	**C (%)**	**O (%)**	**Si(%)**	**Cr(%)**	**Ni(%)**	**Mo(%)**	**Mn(%)**	**Fe (%)**
GA - Fine	0.01	0.03	0.45	17.8	11.4	2.60	1.40	Balanced
WA - Fine	0.02	0.22	0.84	18.1	13.1	2.68	0.05	Balanced
GA - Coarse	0.03	0.06	0.46	16.7	11.1	2.47	1.32	Balanced
WA - Coarse	0.02	0.20	0.84	18.1	13.1	2.68	0.05	Balanced
ASTM F3184	$\leq$0.03		$\leq$1.0	16-18	10-14	2-3	$\leq$2	

The SEM images clearly show the differences in terms of morphology between the two atomization processes: GA powders are characterized by quasi-spherical shape and presence of satellites on the surface, while WA ones show irregular shape with rough edges.

The chemical composition of the two powders shows a different Oxygen content as expected. The higher presence of Oxygen in Stainless Steel powders produced via WA powders has been already reported in [25] and [26] and for 17-4 PH by [8] and it is due to the reaction of the molten material with the atomization medium. The WA powders used in this experimentation are characterized by an Oxygen content 4 times higher than GA, this could have an impact on the processability and, eventually, on the final part properties of the SLM parts. Another difference between WA and GA powders is the Manganese content. The low Mn content in WA powders is supposed to reduce oxide formation and it was already investigated by [27]. Nevertheless,

all four powders comply with the specification for AISI 316L with Powder Bed Fusion processes, ASTM F3184-16.

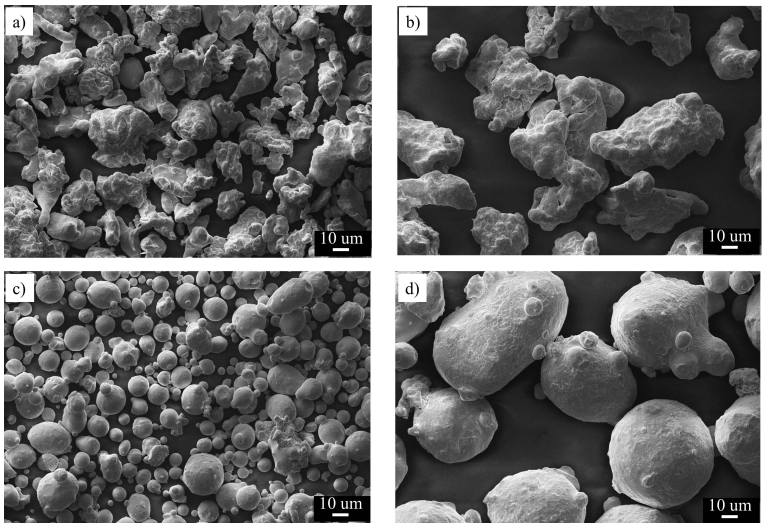

Figure 2: SEM images of the four powders. a) WA- Fine, b) WA-coarse, c) GA-Fine and d) GA-coarse.

The four powders were analyzed in terms of Chromium and Nickel equivalent composition using the Schaeffler diagram [28]. This diagram is used to predict the composition and microstructure of stainless steel weld deposit. Chromium and Nickel equivalent composition are reported in Table 11. We conclude that the four powders are similar from a microstructural point of view.

Table 11: Chromium and Nickel equivalent composition for the four powders using [28].

Powder	**Chromium equivalent (%)**	**Nickel equivalent (%)**
GA - Fine	21.08	12.46
WA - Fine	22.04	13.73
GA - Coarse	19.86	12.66
WA - Coarse	22.04	13.73

5. Results

In the following sections, the results in terms of density and tensile properties for WA and GA powders are showed and discussed.

5.1. Density measurement

WA and GA powders are compared considering the same layer thickness and particle fraction. Although the interval of volumetric energy density used is the same, the four batches of powder exhibit different behaviors in terms of SLM processability. For this reason, each combination of powder fraction and layer thickness is discussed in separate paragraphs. The results are showed in Figure 3.

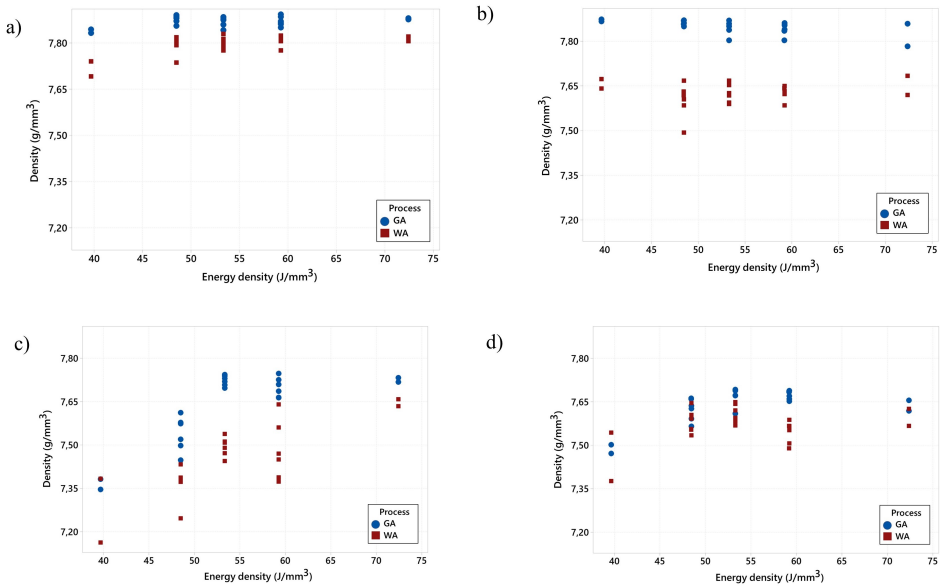

Figure 3: Density results a) Fine fractions at z=50 µm b) Fine fractions at z=50 µm c) Coarse fractions at z=75 µm d) Coarse fractions at z=75 µm

5.1.1. Fine fractions at z = 50 μm

In this condition, both powders showed an almost steady behavior, as a matter of fact for E_d greater than 48.5 J/mm^3 the density is constant as visible in Figure 3 a). An exception is E_d = 39.7 J/mm^3, where WA samples appear to have a slightly lower density than all other samples. At low energy density, the balling effect has considerable effects on the solidification process, as shown in [29]. The worse solidification of WA powders could be ascribed to the high Oxygen content and worse homogeneity of the powder bed. At 48.5 J/mm^3, one WA sample is characterized by a much lower density compared to its replicate; the sample Treatment is (t,d_p, d_h) = (72 μs, 66 μm, 90 μm). As showed by [9] and [14], localized porosity was found in WA samples likely due to lower powder bed density of irregular particles. In this case, the lower energy density combined with the presence of irregularities on the powder bed might generate defects on the final part.

5.1.2. Fine fractions at z = 75 μm

Increasing the layer thickness to 75 μm amplifies the differences in part density between WA and GA powders. Density results are shown in Figure 3 b). GA powder performed better than WA batch in all experimental conditions. As regards to Figure 3 a), the layer thickness was changed as well as the process parameters according to the procedure described in Section 3.3. The trend of the two powders is the same as volumetric energy density increases, both fractions showing steady behavior. In respect to z = 50 μm, GA powders were characterized by a reduction of porosity of approximately 0.02 g/cm^3. By contrast, the performances of the WA-fine fraction with a high layer thickness were reduced by a greater amount, as the mean difference is 0.17 g/cm^3. The workability of the smaller fraction of the

powders at higher layer thickness (and therefore at higher productivity rate) is showed by the good density values obtained by the GA batch. Similarly with the previous case, for energy density equal to 48.5 J/mm^3 one WA sample resulted in a low density. The position on the building platform of these two samples is different, so the only possible explanation for this behavior is the combination of low energy density with localized irregularities on the powder bed.

5.1.3. Coarse fraction at z = 50 μm

In Figure 3 c), the results of coarse fractions at small layer thickness are presented. For this case as well, GA batch performed better than WA. WA samples were characterized by a steady increase in density with increasing energy density. The maximum density reached for coarse WA powders and z=50 μm was 7.66 g/cm^3. However, not even GA fraction achieved full densification. Within the range of E_d evaluated, GA powder appears to reach a steady level at 53.3 J/mm^3 with a density of 7.75 g/cm^3, which is much lower than 7.89 g/cm^3, that is, the mean density reached by the fine fraction for the same layer thickness value. This could be attributed to the fact that the PSD of this powder is much higher than the layer thickness, even considering the effective layer thickness as defined by [18]. It is possible that most of the particles were removed by the powder bed due to their large diameter compared to the layer thickness, leaving the powder bed with only small particles that could not ensure a good powder bed density. WA samples were characterized by high porosity, similar to the one produced with small PSD and high layer thickness. Pores found in WA-coarse at small layer thickness were large and irregular: some are flat lying on single layers while others spread across many hundreds of microns. A 3D reconstruction

of the best coarse-WA powder fraction at small layer thickness is shown in Figure 7 b). It is clear that two very different porosity structures were obtained: the difference in the solidification process is marked even though the volumetric energy density used is quite similar.

5.1.4. Coarse fractions at z = 75 μm

Coarse fractions with z = 75 μm are the combination that generates the worst results in terms of density and the results are presented in Figure 3 d). In this case, the difference between GA and WA powders is much less pronounced. GA powders reached their maximum density of 7.70 g/cm^3 with E_d = 59.2 J/mm^3, while the highest density for WA was reached at 53.3 J/mm^3 with a value of 7.65 g/cm^3.

The presence of large void regions might indicate an inhomogeneous powder layering. However, since this defect is present in both powders the cause should not be ascribed to the lower flowability of the WA powders. It is likely that the large particles and the high layer thickness avoided the bonding between consecutive layers, due to lower absorption [30].

5.2. X-ray computed tomography and cross sections

5.2.1. Fine fractions

The least dense sample from WA fine fraction and z= 50 μm is showed in Figure 4 a) and c) and it is characterized by irregular porosity that spans across several layers along the building direction, the dimension of these pores were up to 300 μm. Due to their shape, it is plausible to attribute them to lack of fusion phenomena, [31], [32]. Porosity due to lack of fusion defects in AISI316L SLM parts were also showed by [33], [34] and [35] at low energy density values. Reconstruction of the best WA sample produced

at $E_d = 53.3$ J/mm^3 and z= 50 µm showed few spherical porosities and it is reported in Figure 4 b) while SEM cross sections of some defects are showed in Figure 4 d). Small spherical pores were also found in optimal condition by other authors,[34], [36] and [33]. 3D reconstruction of samples produced with GA fine powder with z= 50 µm showed few small spherical pores, an example of pore is found on a cross section is showed in Figure 5. Most of the pores found on the SEM cross section of GA samples were spherical with a diameter of approximately 20-30 µm.

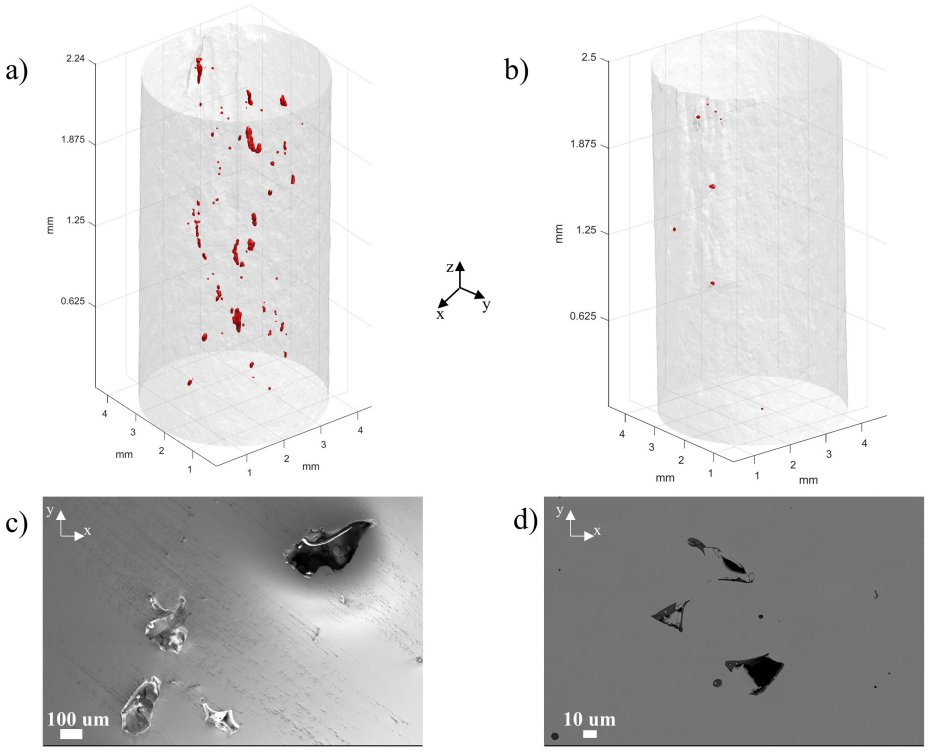

Figure 4: 3D reconstruction of worse and best sample from WA powders at z = 50 µm a) Worse sample at $E_d = 39.7$ J/mm^3. b) Best sample at $E_d = 53.3$ J/mm^3. SEM cross sections of worse and best sample from WA powders at z = 50 µm c) Worse sample at $E_d = 39.7$ J/mm^3 d) Best sample at $E_d = 53.3$ J/mm^3.

GA samples showed very low porosity from XCT reconstruction and therefore the reconstruction images are not shown. Pores found on the SEM cross section of the GA samples were similar to the ones showed in Figure 5 in terms of both size and shape. In Figure 6, the XCT 3D reconstruction of the best sample produced with E_d = 39.6 J/mm^3 with WA powder is showed. Pores in this sample were characterized by an irregular shape and a wide span along the building direction (Figure 6 b)). This behavior might be due to low powder packing density for large layer thickness, which produced an irregular powder bed density and, eventually, large cavities that were not filled with powder. Moreover, according to the work of Li et al. [29], not only the oxygen content but also the increased layer thickness could enhance the balling phenomena, which, eventually, reduces the quality of the powder bed as shown by the high surface roughness of the WA samples. These pores were similar in shape and in size (up to 300 µm) with the defects showed in Figure 4 c).

Figure 5: SEM cross section of GA sample (fine fraction) produced at 53.3 J/mm^3 and z = 50 µm.

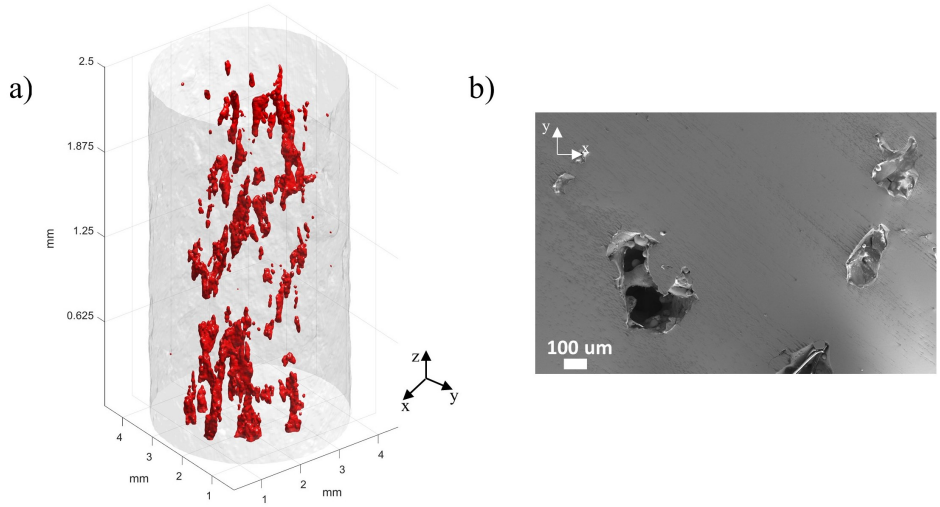

Figure 6: XCT reconstruction a) and SEM cross section b) of WA sample using fine fraction powder at E_d = 39.6 J/mm^3 and z=75 µm

5.2.2. Coarse fractions

In Figure 7 a), the 3D reconstruction of the best GA sample produced at 53.3 J/mm^3 using the coarse fraction and z = 50 µm is showed. The amount of porosity found is clearly higher compared to the previous cases and also different types of pores are visible: small-spherical and also large-irregular as visible in Figure 7 c). As the cross-section of the best GA sample is characterized by wide areas of good densification, the irregular pores identified could be attributed to powder properties rather than unsuitable process parameters (Figure 7c)). Small pores were in the range of 10-50 µm, as in the previous cases.

The best sample for WA and GA coarse powders using z = 75 µm showed quite a similar porosity structure: big voids with irregular shape across multiple layers. Cross sections of the two samples are shown in Figure 8.

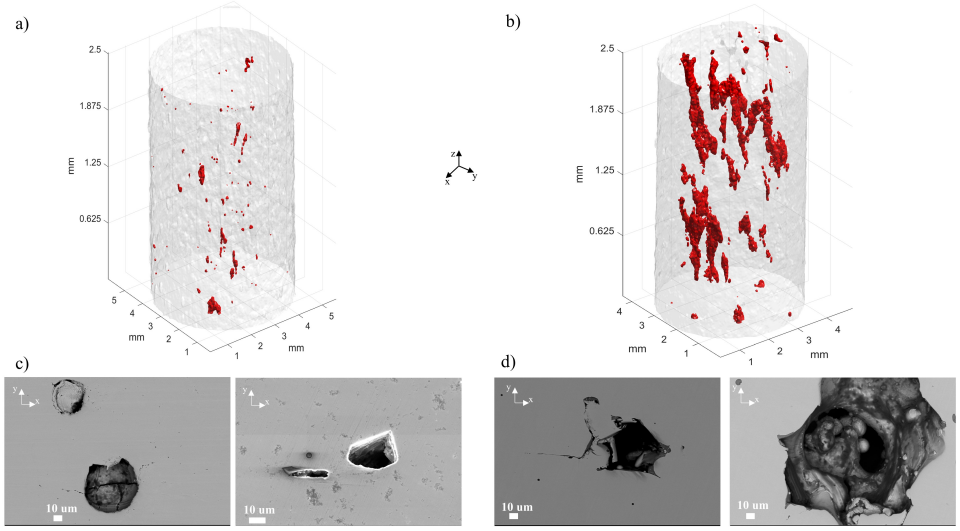

Figure 7: 3D reconstruction of best samples produced with coarse fractions at z=50 µm. a) GA sample produced at E_d = 59.3 J/mm^3. b) WA sample produced at E_d = 53.3 J/mm^3. SEM cross sections of c) GA sample produced at E_d = 59.3 J/mm^3. d) WA sample produced at E_d = 53.3 J/mm^3.

Both samples are characterized by unmelted particles inside the voids, which are clearly visible from SEM images in Figure 8 c) and d).

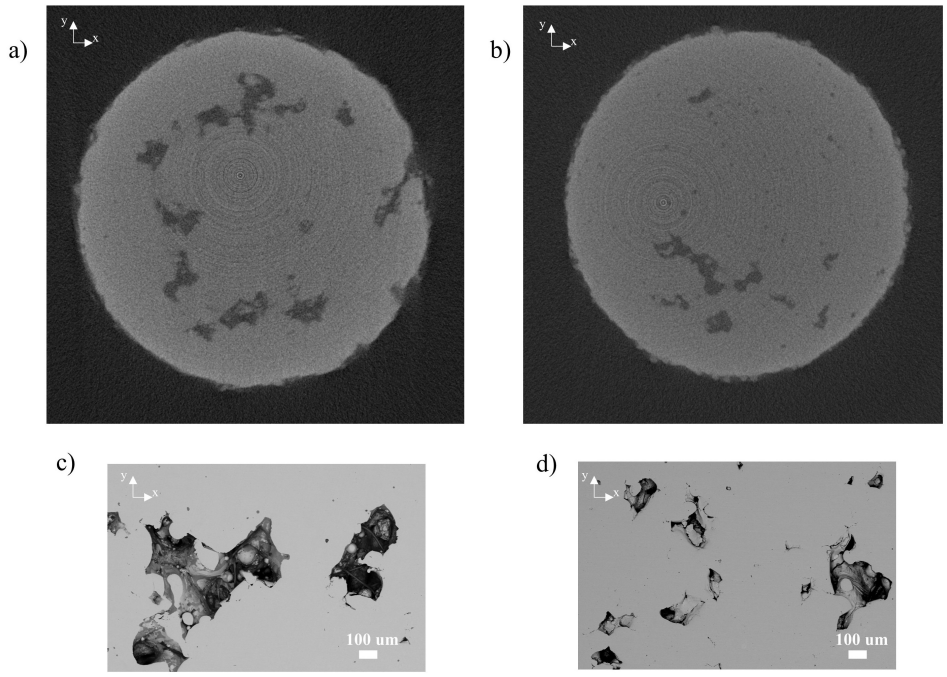

Figure 8: a) XCT slice of best coarse WA batch with z=75 µm b) XCT slice of best coarse GA batch c) SEM cross section of best coarse WA batch with z=75 µm d) SEM cross section of best coarse GA batch with z=75 µm

5.3. Comments on density results

Hereunder, some comments based on the part density results are reported:

- The density results show that the workability of the fine fraction is acceptable only when the layer thickness is 50 μm. By increasing z, there is a reduction of the part density, especially for WA batch. It is likewise interesting to notice that the optimal conditions for AISI 316L suggested by the machine manufacturer are also the best for the powders produced by other suppliers.

- The coarser fraction could not achieve high part density, irrespective of the layer thickness used. It is possible that the worse behaviour of the powders at z = 75 μm is due to the choice of individual process parameters, as there is not a linear correspondence between the solidification and energy density as layer thickness is changed.

- The relationship between PSD and layer thickness is still unclear, as the GA - fine batch resulted in good part density even at 75 μm. A possible explanation might be due to the higher apparent density and consequent packing density of GA powders. Moreover, the reduced oxygen content might have increased the workability of the GA powders.

- An interesting result is that the highest density was achieved for both powders in the same condition: low layer thickness and fine fraction. In this condition, WA powders achieved full density at a higher value of energy density (47 J/mm^3) than GA powders (40 J/mm^3). However, this result is in contrast with the findings of [37] using Ti6Al4V

alloy, where as layer thickness is increased the optimal energy density decreases. Further investigation is needed to understand how the higher presence of oxygen on WA powders impacts on the processability, according to [36] the presence of an oxide layer on the surface of the particles enhances their absorptivity. However, the result of this work showed that WA powders require more energy to achieve full densification. This discrepancy might be attributed to the excessive presence of oxygen which induces porosity on the final part [29] or to the decreased flowability and packing density of WA powders. A possible explanation for the difference in part density between WA and GA samples is the highest apparent density of the GA powders. According to [24] and [38], the higher the apparent density the higher the packing density of the powder bed, which eventually leads to lower porosity in the final part.

- The optimality range for both WA and GA powders is consistent with the results of [39], which also used the same industrial system of the present work (Renishaw AM250). Within the 48 - 60 range J/mm^3 the difference between GA and WA is not relevant, as indeed the best samples show similar porosity structures. The optimal Energy density range for Fine fraction with z = 50 μm is also similar to the works by [36],[34], [40] and [41] using a different SLM system.

5.4. Tensile tests

The highest density for GA and WA powders was achieved using fine fractions at z=50 μm, and the optimal interval of energy density is 48-60 J/mm^3. As shown elsewhere [42], in the steady region of the parameters, i.e. where part density does not change with increasing energy density, the

static properties do not depend on the individual process parameters used. Accordingly, based on the results shown in Figure 3 a), we could use one combination of parameters (t, d_p, d_h) belonging to the steady interval to produce tensile specimen. From the density results, one outlier was detected for WA powders at 48.5 J/mm^3 at z=50 μm; therefore, this level of energy density was not selected to build tensile specimens. We opted to choose the combination ensuring highest productivity and belonging to the steady region; this condition is the center point of the factorial design (in Table 4), which is also the Renishaw suggested condition for AISI 316L.

The number of specimens was determined based on a statistical calculation to ensure a power of the test of the difference of UTS between GA and WA of at least 90%; that is impliedly accepting a probability of 10% of not identifying a difference between the two batches when it actually exists. The difference of interest was defined as ± 5% of the UTS for stainless steel 316L based on ASTM A276/A276M17, i.e. 550 MPa; the standard deviation of the process was estimated from previous tensile tests with AISI 316L on the Renishaw machine (σ=10 MPa). As a result, 5 tensile specimens for each powder were built.

An example of a build of tensile specimens is shown in Figure 9. Tensile properties are characterized in terms of ultimate tensile strength UTS and elongation after fracture E%.

The density of the tensile samples was measured to verify the consistency of the process; the results are reported in Table 12. The mean densities of tensile samples are in harmony with the results obtained with the small cylindrical samples analyzed in the previous section. It is once again verified that GA samples are characterized by higher density compared to WA. As shown by [43] for Ti6Al4V alloy, tensile properties depend on the presence

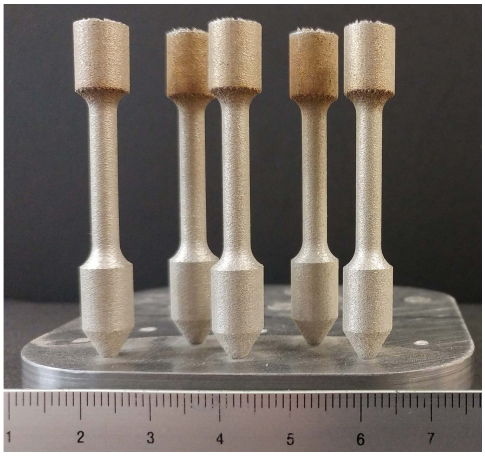

Figure 9: Example of build of tensile specimen, dimensions are reported in Table 3.

of porosity, even when at a low level ($< 1\%$). By analyzing the results of the tensile tests, it will be possible to verify whether or not the differences in terms of density for WA and GA samples result in different tensile properties.

Table 12: Density of tensile specimen (results based on 5 samples for each powder).

Production process	**Mean density**, g/cm^3	**Standard deviation**, g/cm^3
GA	7.88	0.005
WA	7.82	0.009

In Table 13 we list the tensile properties for all the samples investigated. Levene's test for equal variances indicates that there is not statistical evidence to conclude that the variability of the tensile results is different between WA and GA powders (p-value 0.453 for UTS and 1.000 for elongation). Performing a two-sample t-test, we conclude that there is no statistical difference between WA and GA samples both in terms of UTS and elongation; the p-values of the test are 0.422 and 0.351 respectively. The yield strength

Table 13: UTS and elongation after fracture of WA and GA samples.

	UTS [MPa]	
	WA	GA
	600	602
	599	597
	597	599
	608	598
	601	600
Mean	601	599
St.Dev	4.2	1.9

	El [%]	
	WA	GA
	25	20
	20	15
	20	15
	15	20
	20	20
Mean	20	18
St.Dev	3.5	2.7

(YS) for GA samples was 443 ± 3.1 MPa, while for WA samples was 477 ± 3.8 MPa.

Standard ASTM F3184-16 (Additive Manufacturing Stainless Steel Alloys with Powder Bed Fusion) does not provide reference mechanical properties for the "as-built" condition. For the solution annealed or the stress relieved condition, the expected tensile properties are UTS=515 MPa, YS=205 MPa and elongation=30%. Compared to the standard, in this work we obtained a higher UTS and a lower elongation, that is coherent with the absence of post-processing. The results of the present work fit well with the result of [39] in which the same industrial machine and 316L gas-atomized powders were used. In [39] the tensile results for the "as-built" samples were UTS=524 MPa, YS=385 Mpa and elongation 22%.

In conclusion, the results of this experimental campaign show that the tensile properties are comparable with the literature and with the reference standard for the SLM process as summarized in Table 14.

The fractographic images of GA and WA samples show that the fracture is ductile with the presence of large dimples on the surface; dimples are indicated by white arrows in Figure 10. On the surfaces, there was no

Table 14: Summary of tensile properties of 316L processed with SLM.

Source	**UTS**, **MPa**	**UTS**, **MPa**	**El**,%
This work (GA)	599	443	18
This work (WA)	601	477	20
Lavery et al. [39]	524	385	22
ASTM F3184 - Solution annealed or stress relieved	515	205	30

evidence of large defects or unmelted particles.

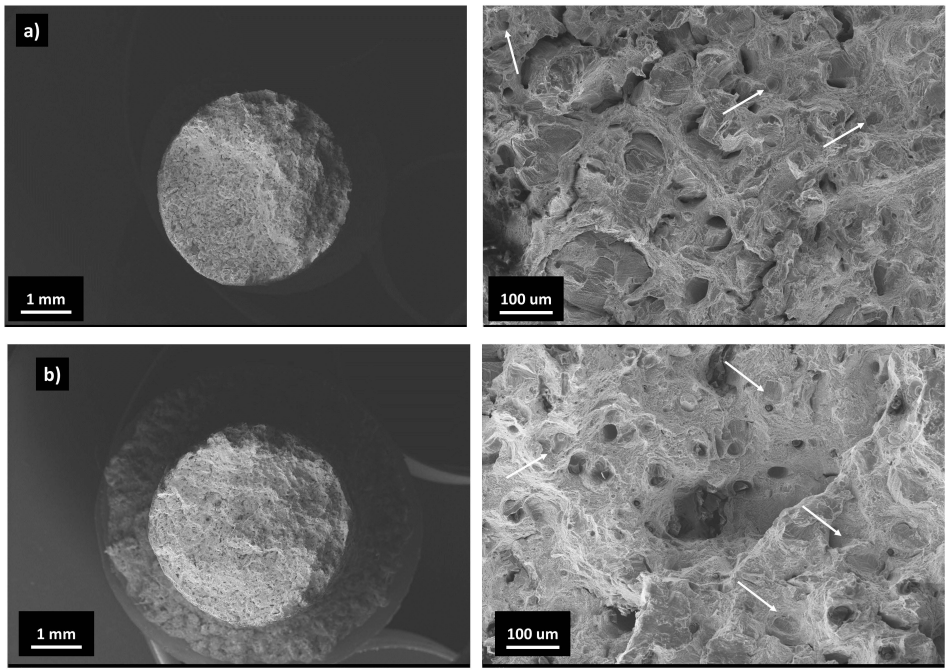

Figure 10: Fractographic images of tensile specimen produced with different powders. a) water atomized, b) gas atomized.

6. Conclusions

In this work, we investigated the influence of the atomization medium and the particle size distribution on the final part density at different layer

thickness values. The same volumetric energy density was used at z = 50μm and z = 75 μm by linearly scaling the process parameters. The results showed that:

- It is possible to obtain samples with high density using less expensive WA stainless steel powders;
- High density is obtained using the fine fraction at a low level of layer thickness. In this condition, GA density was steady within 40 - 72 J/mm^3 range, while WA reached the highest density at E_d, i.e. 48 J/mm^3;
- The lower apparent density of WA powders could explain the lower density of WA samples, even when using optimal process parameters;
- Using the condition which maximizes density for both powders, the porosity structure measured with X-ray Computed Tomography was similar for WA and GA samples;
- The solidification of the same powder at two different layer thicknesses shows different mechanisms, despite using the same volumetric energy density. This result suggests that volumetric energy density does not provide information about the densification behavior of a powder if the layer thickness is changed;
- UTS is not statistically different among the two powders considered (WA-fine and GA-fine);

Future work will address the problem of improving the workability of irregular powders and the study of powder batches coming from different manufacturers analyzing how their processability changes, given the same

material and the same atomization medium. Moreover, the choice of the value of layer thickness based on the powder properties and PSD should be further developed. Future analysis will be focused on the relationship between the porosity structure (position, size and, shape of pores) with static properties.

Acknowledgment

The authors would like to thank Pometon SpA for supplying water atomized powders. This work was partially founded by European Union, Repubblica Italiana, Regione Lombardia and FESR for the project MADE4LO under the call "POR FESR 2014-2020 ASSE I - AZIONE I.1.B.1.3.

References

[1] H. Gong, K. Rafi, H. Gu, T. Starr, B. Stucker, Analysis of defect generation in ti–6al–4v parts made using powder bed fusion additive manufacturing processes, Additive Manufacturing 1 (2014) 87–98.

[2] J. H. Rao, Y. Zhang, X. Fang, Y. Chen, X. Wu, C. H. Davies, The origins for tensile properties of selective laser melted aluminium alloy a357, Additive Manufacturing 17 (2017) 113–122.

[3] Y. Bai, Y. Yang, Z. Xiao, M. Zhang, D. Wang, Process optimization and mechanical property evolution of alsimg0. 75 by selective laser melting, Materials & Design 140 (2018) 257–266.

[4] Y. Liu, J. Zhang, Z. Pang, W. Wu, Investigation into the influence of laser energy input on selective laser melted thin-walled parts by re-

sponse surface method, Optics and Lasers in Engineering 103 (2018) 34–45.

[5] W. J. Sames, F. List, S. Pannala, R. R. Dehoff, S. S. Babu, The metallurgy and processing science of metal additive manufacturing, International Materials Reviews 61 (5) (2016) 315–360.

[6] J. A. Slotwinski, E. J. Garboczi, Metrology needs for metal additive manufacturing powders, JOM 67 (3) (2015) 538–543.

[7] J. H. Tan, W. L. E. Wong, K. W. Dalgarno, An overview of powder granulometry on feedstock and part performance in the selective laser melting process, Additive Manufacturing 18 (2017) 228–255.

[8] H. Irrinki, M. Dexter, B. Barmore, R. Enneti, S. Pasebani, S. Badwe, J. Stitzel, R. Malhotra, S. V. Atre, Effects of powder attributes and laser powder bed fusion (L-PBF) process conditions on the densification and mechanical properties of 17-4 PH stainless steel, JOM 68 (3) (2016) 860–868.

[9] R. Engeli, T. Etter, S. Hoevel, K. Wegener, Processability of different IN738LC powder batches by selective laser melting, Journal of Materials Processing Technology 229 (2016) 484–491.

[10] C. Lindemann, U. Jahnke, M. Moi, R. Koch, Analyzing product lifecycle costs for a better understanding of cost drivers in additive manufacturing, in: 23th Annual International Solid Freeform Fabrication Symposium–An Additive Manufacturing Conference. Austin Texas USA 6th-8th August, 2012.

[11] M. Baumers, L. Beltrametti, A. Gasparre, R. Hague, Informing additive manufacturing technology adoption: total cost and the impact of capacity utilisation, International Journal of Production Research 55 (23) (2017) 6957–6970.

[12] A. T. Sutton, C. S. Kriewall, M. C. Leu, J. W. Newkirk, Powder characterisation techniques and effects of powder characteristics on part properties in powder-bed fusion processes, Virtual and Physical Prototyping 12 (1) (2017) 3–29.

[13] M. N. Ahsan, A. J. Pinkerton, R. J. Moat, J. Shackleton, A comparative study of laser direct metal deposition characteristics using gas and plasma-atomized Ti-6Al-4V powders, Materials Science and Engineering:A 528 (25-26) (2011) 7648–7657.

[14] E. Olakanmi, Selective laser sintering/melting (sls/slm) of pure al, al–mg, and al–si powders: Effect of processing conditions and powder properties, Journal of Materials Processing Technology 213 (8) (2013) 1387–1405.

[15] A. Y. Alfaify, J. Hughes, K. Ridgway, Critical evaluation of the pulsed selective laser melting process when fabricating Ti64 parts using a range of particle size distributions, Additive Manufacturing 19 (2018) 197–204.

[16] M. Letenneur, V. Brailovski, A. Kreitcberg, V. Paserin, I. Bailon-Poujol, Laser powder bed fusion of water-atomized iron-based powders: process optimization, Journal of Manufacturing and Materials Processing 1 (2) (2017) 23.

[17] S. Cacace, A. G. Demir, Q. Semeraro, Densification mechanism for different types of stainless steel powders in selective laser melting, Procedia CIRP 62 (2017) 475–480.

[18] A. B. Spierings, N. Herres, G. Levy, Influence of the particle size distribution on surface quality and mechanical properties in AM steel parts, Rapid Prototyping Journal 17 (3) (2011) 195–202.

[19] K. Guan, Z. Wang, M. Gao, X. Li, X. Zeng, Effects of processing parameters on tensile properties of selective laser melted 304 stainless steel, Materials & Design 50 (2013) 581–586.

[20] M. Ma, Z. Wang, M. Gao, X. Zeng, Layer thickness dependence of performance in high-power selective laser melting of 1Cr18Ni9Ti stainless steel, Journal of Materials Processing Technology 215 (2015) 142–150.

[21] Z. Hu, H. Zhu, H. Zhang, X. Zeng, Experimental investigation on selective laser melting of 17-4PH stainless steel, Optics & Laser Technology 87 (2017) 17–25.

[22] V. S. Sufiiarov, A. Popovich, E. Borisov, I. Polozov, D. Masaylo, A. Orlov, The effect of layer thickness at selective laser melting, Procedia engineering 174 (2017) 126–134.

[23] W. E. King, H. D. Barth, V. M. Castillo, G. F. Gallegos, J. W. Gibbs, D. E. Hahn, C. Kamath, A. M. Rubenchik, Observation of keyhole-mode laser melting in laser powder-bed fusion additive manufacturing, Journal of Materials Processing Technology 214 (12) (2014) 2915–2925.

[24] H. Irrinki, J. S. D. Jangam, S. Pasebani, S. Badwe, J. Stitzel, K. Kate, O. Gulsoy, S. V. Atre, Effects of particle characteristics on the mi-

crostructure and mechanical properties of 17-4 PH stainless steel fabricated by laser-powder bed fusion, Powder Technology 331 (2018) 192–203.

[25] A. Simchi, Direct laser sintering of metal powders: Mechanism, kinetics and microstructural features, Materials Science and Engineering: A 428 (1-2) (2006) 148–158.

[26] R. Li, Y. Shi, Z. Wang, L. Wang, J. Liu, W. Jiang, Densification behavior of gas and water atomized 316L stainless steel powder during selective laser melting, Applied surface science 256 (13) (2010) 4350–4356.

[27] M. Tobar, J. Amado, J. Montero, A. Yáñez, A study on the effects of the use of gas or water atomized aisi 316l steel powder on the corrosion resistance of laser deposited material, Physics Procedia 83 (2016) 606–612.

[28] A. L. Schaeffler, Constitution diagram for stainless steel weld metal, Metal progress 56 (11) (1949) 680.

[29] R. Li, J. Liu, Y. Shi, L. Wang, W. Jiang, Balling behavior of stainless steel and nickel powder during selective laser melting process, The International Journal of Advanced Manufacturing Technology 59 (9-12) (2012) 1025–1035.

[30] C. Boley, S. Khairallah, A. Rubenchik, Calculation of laser absorption by metal powders in additive manufacturing, Applied optics 54 (9) (2015) 2477–2482.

[31] F. Kim, S. Moylan, E. Garboczi, J. Slotwinski, Investigation of pore structure in cobalt chrome additively manufactured parts using x-ray computed tomography and three-dimensional image analysis, Additive Manufacturing 17 (2017) 23–38.

[32] G. Kasperovich, J. Haubrich, J. Gussone, G. Requena, Correlation between porosity and processing parameters in tial6v4 produced by selective laser melting, Materials & Design 105 (2016) 160–170.

[33] J. Cherry, H. Davies, S. Mehmood, N. Lavery, S. Brown, J. Sienz, Investigation into the effect of process parameters on microstructural and physical properties of 316l stainless steel parts by selective laser melting, The International Journal of Advanced Manufacturing Technology 76 (5-8) (2015) 869–879.

[34] M. Zhang, C.-N. Sun, X. Zhang, P. C. Goh, J. Wei, D. Hardacre, H. Li, Fatigue and fracture behaviour of laser powder bed fusion stainless steel 316l: influence of processing parameters, Materials Science and Engineering: A 703 (2017) 251–261.

[35] E. Liverani, S. Toschi, L. Ceschini, A. Fortunato, Effect of selective laser melting (slm) process parameters on microstructure and mechanical properties of 316l austenitic stainless steel, Journal of Materials Processing Technology 249 (2017) 255–263.

[36] J. Yan, Y. Zhou, R. Gu, X. Zhang, W.-M. Quach, M. Yan, A comprehensive study of steel powders (316l, h13, p20 and 18ni300) for their selective laser melting additive manufacturing, Metals 9 (1) (2019) 86.

[37] M. Letenneur, A. Kreitcberg, V. Brailovski, Optimization of laser pow-

der bed fusion processing using a combination of melt pool modeling and design of experiment approaches: Density control, Journal of Manufacturing and Materials Processing 3 (1) (2019) 21.

[38] H. Zhu, J. Fuh, L. Lu, The influence of powder apparent density on the density in direct laser-sintered metallic parts, International Journal of Machine Tools and Manufacture 47 (2) (2007) 294–298.

[39] N. Lavery, J. Cherry, S. Mehmood, H. Davies, B. Girling, E. Sackett, S. Brown, J. Sienz, Effects of hot isostatic pressing on the elastic modulus and tensile properties of 316l parts made by powder bed laser fusion, Materials Science and Engineering: A 693 (2017) 186–213.

[40] E. Yasa, J.-P. Kruth, Microstructural investigation of selective laser melting 316l stainless steel parts exposed to laser re-melting, Procedia Engineering 19 (2011) 389–395.

[41] P. Krakhmalev, G. Fredriksson, K. Svensson, I. Yadroitsev, I. Yadroitsava, M. Thuvander, R. Peng, Microstructure, solidification texture, and thermal stability of 316 l stainless steel manufactured by laser powder bed fusion, Metals 8 (8) (2018) 643.

[42] S. Cacace, Q. Semeraro, About fluence and process parameters on maraging steel processed by selective laser melting: Do they convey the same information?, International Journal of Precision Engineering and Manufacturing 19 (12) (2018) 1873–1884.

[43] T. Voisin, N. P. Calta, S. A. Khairallah, J.-B. Forien, L. Balogh, R. W. Cunningham, A. D. Rollett, Y. M. Wang, Defects-dictated tensile prop-

erties of selective laser melted ti-6al-4v, Materials & Design 158 (2018) 113–126.